Article

pH-Triggered Poly(ethylene glycol)−Poly(lactic acid/glycolic acid)/Croconaine Nanoparticles-Assisted Multiplexed Photoacoustic Imaging and Enhanced Photothermal Cancer Therapy

Shiying Li,[†] Kwok-Ho Lui,[†] Xin Li, Xueyang Fang, Wai-Sum Lo, Yan-Juan Gu,* and Wing-Tak Wong*

Read Online

ACCESS | Metrics & More | Article Recommendations | Supporting Information

ABSTRACT: The most advantageous and attractive property of photoacoustic imaging is its capability to visualize and differentiate multiple species according to their unique absorbance profiles simultaneously in a single mixture. We here report the pH-sensitive near-infrared (NIR) croconaine (Croc) dyes-loaded copolymeric PEG−PLGA nanoparticles (NPs) for in vivo multiplexed PA imaging and pH-responsive photothermal therapy (PTT) in an orthotopic xenograft model. PEG chains on the polymeric NPs shell were conjugated with iRGD in another set of NPs to realize efficient tumor targeting. The distribution and the intensity of two sets of iRGD-targeted and nontargeted NPs inside tumors are simultaneously imaged and monitored in vivo. Meanwhile, the utilization of iRGD-targeted PPC$_{815}$ NPs as a pH-active photo-thermal agent with promising tumor-inhibition efficacy was demonstrated. As a result, this nanoplatform is capable of assisting multiwavelength unmixing of PA imaging as well as providing remarkable photothermal ablation for anticancer treatment.

KEYWORDS: multiplexed photoacoustic imaging, spectra unmixing, PEG−PLGA nanoparticles, photothermal therapy, orthotopic xenograft model
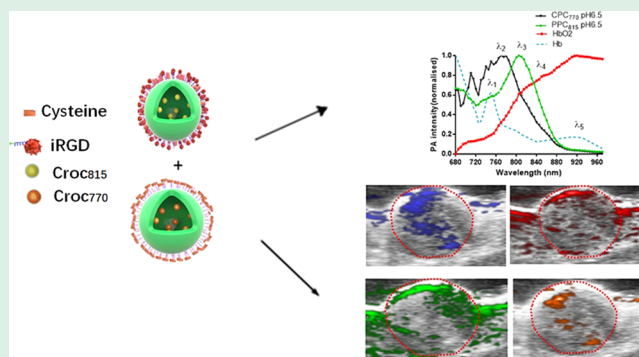
1. INTRODUCTION

Photoacoustic (PA) imaging has recently been employed as an attractive tool for noninvasive diagnosis due to its noninvasive nature and rapid acquisition process.[1−3] Moreover, PA imaging provides high-resolution optical images and deep penetration where classic conventional optical imaging techniques struggle.[4−6] Promising efforts have been devoted to developing novel contrast agents to achieve higher-quality PA images.[7−10] However, the two main light absorbers in biological tissues, hemoglobin and melanin, can also act as endogenous molecules to generate PA signals at 750/850 nm that cannot be distinguished from one another in a single image.[11−13] To further simplify the signal-resolution process to deconvolute the photoabsorbing substances of interest via their readily tuned absorption spectra, multiplexed PA imaging is utilized on the biological tissues to create multiple frames at different wavelengths, and the spectra unmixing algorithm is applied to one image to resolve the biomarker of interest.[14] Multiplexed imaging is a useful tool to spatially define and distinguish specific intrinsic molecules or extrinsically administered agents simultaneously based on their absorption spectra. These functions are typically powerful for assessing the binding and targeting capabilities of nanoparticles (NPs) in targeted drug-delivery systems, pH mapping of tumors, and multiscale imaging of in vivo dynamics.[14−20]

Despite this potential of PA imaging, the attenuation of wavelength in deep tissue imaging remains a major obstacle.[21] There are a few reports on using NPs loaded with organic dyes with narrow and sharp absorption peaks in the NIR wavelength region.[22,23] The simultaneous imaging of untargeted Par788 and folate-targeted fol-Par900 NPs, both tagged with a unique optical dye, was demonstrated.[23] Gold nanorods are the most frequently utilized contrast agent as multiplexed photo-absorbing substances due to their tunable optical absorption property, but they are restricted by intrinsically broad absorbance spectra and weak spectral separability in NIR region.[24−26] The difficulty of developing novel probes for multiplexed PA imaging lies in optimizing the structure and absorbance profiles of the chromophore in order to limit the overlap of PA intensity and eliminate the drawbacks of wavelength-dependent light attenuation in deep tissue penetration depths.

The discovery and understanding of tumor environment (TME) in tumor progression has led to the emergence of diagnostic techniques and therapeutic agents with enhanced specificity toward TME.[9,27−30] It is well-known that the tumor possesses a unique acidosis feature. The alteration of metabolic state in tumor tissue results in peculiar extracellular chemical composition, which leads to the TME being slightly more acidic (pH 6.5−7.0) than normal tissues.[31] The absorption of some NIR organic dyes could be readily tuned in the acidic environment, thus proving to be potentially pH-sensitive PA contrast agents.[32−34] Recently, pH-sensitive Croc dyes exhibited strong NIR absorption and intense photothermal conversion efficiency with remarkable chemical and thermal stability, making them a promising agent for PA as well as PTT.[35−39] However, their poor solubility in aqueous solution hinders *in vivo* biomedical use.[39] There are reports on chemical modification of Croc dyes to improve their biocompatibility through self-assembled HSA-Croc NPs and PEGylation of CR780 (a Croc dye) NPs for PA imaging and PTT.[40,41]

On the other hand, polymeric NPs have been used as drug carriers for tumor imaging and chemotherapy due to their impressive biocompatibility. As an FDA-approved biomaterial, a high degree of biodegradability endows poly(lactic acid/glycolic acid) (PLGA) as a drug carrier, which degrades into nontoxic lactic acid *in vivo*.[42,43] The hydrophilic block of poly(ethylene glycol) (PEG) could extend the systemic circulation time and reduce the nonspecific uptake in healthy tissue.[44−47] Nevertheless, until now, there is very limited information on the methodology of Croc incorporation into PEG−PLGA copolymers. No previous study has attempted to engineer clinically used Croc-loaded PEGylated PLGA for targeted PA imaging and treatment of tumors.

In this work, Croc-loaded copolymeric PEG−PLGA NPs were constructed by means of emulsion−solvent evaporation for *in vivo* multiplexed PA imaging of tumor and photothermal therapy (PTT) as illustrated in Figure 1. Two pH-sensitive Croc derivatives with varying absorbance maxima in the NIR region were synthesized. $Croc_{770}$ and $Croc_{815}$ were encapsulated into the Mal−PEG−PLGA NPs to form a set of nontargeting CPC_{770} NPs and a set of iRGD-targeted PPC_{815}

NPs, respectively. The Mal−PEG−PLGA serves as a protective carrier for Croc delivery and prevents undesired interaction with external molecules present in blood, while iRGD surface medication provides precise tumor-targeting property. This delicate design shall allow efficient delivery of pH-sensing Croc to the tumor via intravenous injection. The unmodified CPC_{770} NPs with only PEG steric layers bind with cysteine that passively accumulates tumors. To this end, the strong background optical absorption hinders *in vivo* molecular insight via PA imaging. By incorporating two pH-sensitive dyes and utilizing seven wavelengths in spectral unmixing, our novel system shall overcome the unwanted background and provide a clear spatial distribution of PPC_{815} and CPC_{770}. This clear spatial distribution in return could offer in-depth understanding of the hemodynamic status of the tumor. Furthermore, the targeting property of PPC_{815} NPs enhances the therapeutic efficiency of PTT treatment.[19] In this study, we employed orthotopic xenograft models to investigate and evaluate the PA imaging and hypothermia anticancer treatment ability of our nanoplatforms. We believe these biocompatible and bioeliminable NPs represent a new generation of nanotheranostic platform to perform diagnosis and anticancer treatment synchronously.

2. EXPERIMENTAL SECTION

2.1. Material and Methods. Diblock copolymer maleimide−poly(ethylene glycol)−poly(lactide-*co*-glycolide)−COOH (Mal−PEG−PLGA−COOH, MW of PEG to PLGA 2 000:15 000, molar ratio of PEG to PLGA 25:75, MW = 17 000 Da) and hydrolyzed poly(vinyl alcohol) (PVA, MW = 13 000−23 000 kDa) were purchased from Sigma. Peptide iRGD (95% purity) was purchased from GR Biochem, Ltd. (Shanghai, China).

2.2. Cell Line and Animals. MDA-MB-231 cells were purchased from ATCC. Cell line was cultured in Dulbecco's modifed Eagle medium (DMEM) supplemented with 10% fetal bovine serum (FBS) and 1% penicillin/streptomycin at 37 °C in a humidified atmosphere of 5% CO_2. BALB/c nude mice (female) were required from the Chinese University of Hong Kong at 4−6 weeks of ages and raised in standard housing conditions set by the Hong Kong Polytechnic University Animal Study Committee (Hong Kong). Animal procedures were carried out following the protocol approved by the Ethics Committee of the Special Health Services Department of Health HKSAR Government.

2.3. Preparation of iRGD−PEG−PLGA/Croc₈₁₅ (PPC₈₁₅), Cys−PEG−PLGA/Croc₈₁₅ (CPC₈₁₅), and Cys−PEG−PLGA/Croc₇₇₀ (CPC₇₇₀) NPs. The detailed synthesis and characterization of Croc derivates ($Croc_{815}$ and $Croc_{770}$) are shown in the Supporting Information.[46,47] Briefly, Mal−PEG−PLGA (8 mg) and $Croc_{815}$ dye (4 mg) were codissolved in chloroform (200 μL). The organic phase was added and emulsified with a PVA (1%, w/v, 1.0 mL) aqueous solution using probe sonicator TL-ST150 (Tenlin China). The resulting O/W emulsion was quickly transferred into an aqueous PVA solution (1%, 10 mL) and mixed well at 500 rpm for solvent evaporation. The resultant NPs were concentrated and washed with Milli-Q water with centrifugation to remove unloaded free dye, polymer, and surfactant. Then, Mal−PEG−PLGA/Croc₈₁₅ NPs were conjugated with the iRGD peptide through the interaction between Mal groups of Mal−PEG−PLGA and the thiol group of iRGD for 24 h. The molar ratio of Mal−PEG−PLGA NPs and iRGD used for conjugation was 4:1. Finally, the unreacted Mal groups on the surface of the NPs were quenched using cysteine (Cys). The resulting solution was transferred into ultrafiltration (MWCO 100 kDa) and centrifuged to form the targeted nanoprobe PPC₈₁₅ NPs. NPs were lyophilized using a freeze-dryer overnight.

In the control, the Mal−PEG−PLGA−COOH/Croc₈₁₅ and Mal−PEG−PLGA−COOH/Croc₇₇₀ NPs were formed using the earlier-mentioned protocol, and then an excess amount of Cys was added to
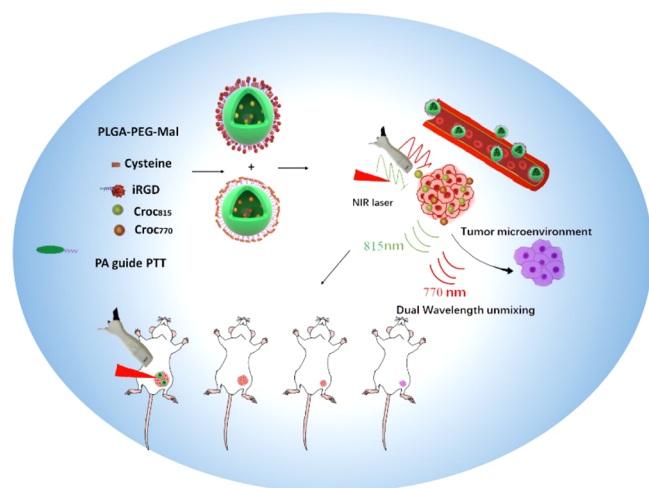

Figure 1. Schematic image of the pH-triggered PEG−PLGA/croconaine nanoparticles for tumor-targeting multiplexed photoacoustic imaging and photothermal therapy in orthotopic xenograft nude mice.

the solution to obtain Cys−PEG−PLGA/Croc$_{815}$ (CPC$_{815}$) and Cys−PEG−PLGA/Croc$_{770}$ (CPC$_{770}$) NPs. High-performance liquid chromatography−mass spectrometry (HPLC-MS) was utilized to analyze the loading capacity (LC%) and encapsulation efficiency (EE %) for Croc dye in NPs. The detailed calculation for Croc dye drug9loading capacity and encapsulation efficiency is shown in the Supporting Information. The loading efficacies of CPC$_{770}$ and PPC$_{815}$ NPs were similar and estimated to be 20.2 and 19.8%, respectively. The encapsulation efficiencies of CPC$_{770}$ and PPC$_{815}$ NPs were about 43.4 and 40.4%, respectively.

2.4. Characterization of PPC$_{815}$, CPC$_{815}$, and CPC$_{770}$ NPs. The morphology and size of NPs were characterized using a JEOL JEM-2011 transmission electron microscope (TEM). UV−vis−NIR absorption spectra of NPs were obtained from pH 5.8, 6.5, 7.4, and 10.0 buffer solution using an Agilent Cary 8454 spectrophotometer. The size and zeta potential of PPC$_{815}$, CPC$_{815}$, and CPC$_{770}$ NPs were analyzed by dynamic light scattering using a Zetasize Nano-ZS90 (Malvern, U.K., He−Ne laser wavelength at 633 nm).

2.5. *In Vitro* Croc$_{815}$ Release from PPC$_{815}$ NPs. To investigate the release of Croc$_{815}$ from PPC$_{815}$ NPs, a fixed amount (1 mg) of each lyophilized PPC$_{815}$ NP was embedded in 2 mL of solution (PBS; pH 7.4, 6.5, and 5.8; ionic strength 0.10 M) at 37 °C under gentle magnetic stirring (300 rpm). For PTT treatment, the laser irradiation was performed at 1.0 W/cm^2 for 5 min. Along different periods, 200 μL of the supernatant was removed and refilled again. The amount of released Croc$_{815}$ was determined using an HPLC-MS system.

2.6. Photothermal Effects of PPC$_{815}$ NPs. To measure the photothermal performance, PPC$_{815}$ NPs (50 μg/mL) in different pH buffer solutions (pH 5.8, 6.5, and 7.4) were irradiated by NIR laser (808 nm, 1.0 W/cm^2, 6 min). Besides, the photothermal stability of PPC$_{815}$ NPs at a concentration of 50 μg/mL was also recorded. The buffer solution containing NPs was irradiated by NIR laser (1.0 W/ cm^2) to its maximum temperature, and then the solution was cooled down naturally; three cycles were repeated, and a thermal imaging camera (Fluke Ti450) was applied to take thermal images.[48] PTT conversion efficiencies (η) of PPC$_{815}$ and CPC$_{770}$ NPs in pH 6.5 buffer solution were obtained by a calculation referring to the recorded temperature curves and experimental details, and the calculations are shown in the Supporting Information. The η of PPC$_{815}$ and CPC$_{770}$ NPs in pH 6.5 buffer solution are 34.7% and 32.0%, respectively.

2.7. Cytotoxicity and Photothermal Effect of PPC$_{815}$ and CPC$_{815}$ *In Vitro*. Breast cancer cells were cultured in 96-well plates and incubated with separate concentrations of PPC$_{815}$ and CPC$_{815}$ NPs in cell dispersion for 24 h. The iRGD block experiment of targeted NPs was performed with preincubation of 10 μL of 0.1 mM iRGD as an inhibitor for 3 h, followed by the same procedures as mentioned earlier. For laser treatment, the cells were treated upon NIR laser (808 nm, 1.0 W/cm^2, 5 min) after a 24 h incubation, followed by incubation for a further 24 h. The evidence of the viability of the cells was shown by CCK-8 assay.

2.8. PA Instrumentation. Photoacoustic and ultrasonic (PA/US) images were performed on a Vevo LAZR-2100 photoacoustic imaging system (FUJIFILM VisualSonics, Canada) equipped with a 21 MHz transducer. The tunable Nd:YAG laser system (OPOTEK, Inc., 680− 980 nm) was used to trigger the acoustic signal acquisition to generate the PA effect.

2.9. PA Signal Measurement of PPC$_{815}$ and CPC$_{770}$ NPs in Tube Phantom. PA spectral scans and images were acquired using tube phantoms that were constructed from 2 cm lengths of polyethylene tubes. The PA signals of PPC$_{815}$ and CPC$_{770}$ nanoprobes (50 μg/mL) in pH 10.0, 7.4, 6.5, and 5.8 PBS buffer were amplified. To each testing solution, 50 μL of a phosphate buffer solution was added (10 mM, 50 μL, 40 °C), and the two nanoprobes were injected into the PE tubes and then posed in the tube phantom under water. Each single wavelength was recorded at 770 and 815 nm threshold images.

2.10. PA Signal Measurement of PPC$_{815}$ and CPC$_{815}$ in Cell Phantom. The MDA-MB-231 were cultured with a density of 1 × 10^5 cells in a 6-well plate. Final concentrations of 50 μg/mL PPC$_{815}$

and CPC$_{815}$ nanoprobes were incubated for 3, 6, 12, and 24 h. Cells were washed with 1× PBS buffer three times. Cells were collected with centrifugation for further experiment. Briefly, the cells were merged with 1% agarose gel with a 1:1 ratio and transferred into a 3D customized mold.

2.11. Animal Model Establishment. To establish the orthotopic xenograft models, nude mice were used for the subcutaneous injection of the 2 × 10^6 MDA-MB-231 breast cancer cells suspended in a total volume of 40 μL of 1:1 medium/matrigel gel into the inguinal gland of the mammary fat pad. When the tumor reached a surface diameter of 4−5 mm, the nude mice were injected with NPs for imaging and therapy.

2.12. *In Vivo* Photoacoustic Imaging. MDA-MB-231 cell-bearing nude mice were injected with the mixture of CPC$_{770}$ and PPC$_{815}$ NPs (1:1, 5 mg/kg per each NP, 200 μL) through intravenous injection. For the control groups, the mice were injected with PPC$_{815}$ NPs alone or CPC$_{815}$ NPs alone with the same dosage. Animals were imaged with the PA system for 72 h. During acquisition, the mice were anesthetized with 3% isoflurane. The 2D/3D ultrasound and PA multispectral images were recorded at designated time intervals at different wavelengths (710, 750, 770, 795, 815, 850, and 890 nm). Spectra unmixing was processed using the Vevo LAZR Software Multiplexer based on PA spectra of CPC$_{770}$ and PPC$_{815}$ NPs (as described before in the PA tube phantom). The PA signals of oxygenated and deoxygenated hemoglobin were multiplexed for more than 50 frames and overlaid on one image.[26] The intensity of the multispectral PA signal of each unmixed absorber was analyzed using Vevo Software. Briefly, the tumor region was outlined as the region of interest (ROI), and each PA intensity signal was quantified using a built-in algorithm. The tumor image with a specific absorber signal was then reconstructed by combining 50 image slides.

2.13. Antitumor Efficacy and Biosafety *In Vivo*. BALB/c nude mice bearing an MDA-MB-231 tumor were equally separately into four groups (n = 4) and intravenously injected with PBS, CPC$_{815}$, CPC$_{815}$ + laser, PPC$_{815}$, and PPC$_{815}$ + laser (5 mg/kg Croc$_{815}$, 200 μL) from their tail vein injection over a period of 14 days when the tumor reached about a surface diameter of 4−5 mm with 50 mm^3 in volume. Clearly, the tumor regions from the two groups of CPC$_{815}$ + laser and PPC$_{815}$ + laser were irradiated by an 808 nm NIR laser at 24 h via intravenous injection (1.5 W/cm^2, 5 min × 3 times). The body weight and tumor size of the mice were measured daily across 2 weeks. The tumor inhibition efficacy was determined by recording the tumor size. The volume of the tumor was calculated according to the formula V = (L × W × W)/2, where L is the larger length and W is the smaller length.[49] The weight of the nude mice was recorded along the whole period to confirm the toxicity of the different groups. Finally, the tumors were harvested and weighed. To further evaluate the toxicity, tumors and main organs of mice were fixed with 4% paraformaldehyde for hematoxylin and eosin (H&E) staining and immunohistochemistical (CD31 staining and TUNEL staining) analyses. Their blood was collected for examination of blood biochemical indexes.

2.14. Statistical Analysis. Statistical comparisons of *in vitro* and *in vivo* data were calculated according to GraphPad Prism 5 software (GraphPad Software, Inc.). Peak intensities were determined between the two groups and statistically compared using ANOVA, with $p < 0.05$ being considered significant.

3. RESULTS AND DISCUSSION

3.1. Fabrication of Nanotheranostics. Two croconaine derivates (Croc$_{815}$ and Croc$_{770}$) with varying absorbance maxima in the NIR region were synthesized according to a previous report. The relevant structure and purity of Croc$_{815}$ and Croc$_{770}$ were confirmed by ^{1}H NMR spectroscopy and mass spectrometry (Figures S1 and S2). Croc$_{815}$ and Croc$_{770}$ have different para-substituents relative to the amine group (nitro and hydrogen groups). Moreover, elemental analysis for Croc$_{770}$ and Croc$_{815}$ confirmed the different structures (Table

Table 1. Physicochemical Characteristics of NPs (Mean ± SEM; n = 3)[a]

nanoparticles	particle size (nm)	PDI	zeta potential (mV)	DL%	EE%
CPC_{770}	182.3 ± 3.0	0.09 ± 0.01	−24.2 ± 2.1	20.2	43.4
CPC_{815}	183.3 ± 2.1	0.10 ± 0.02	−21.2 ± 1.4	19.8	40.4
PPC_{815}	185.1 ± 3.3	0.07 ± 0.03	−1.2 ± 0.7	19.8	40.4

[a]SEM = standard error of mean.

S1). The pH-sensitive NIR absorbances and photothermal performances of $Croc_{815}$ and $Croc_{770}$ dyes are depicted in Figure S3. The nitro group of the benzene ring $Croc_{815}$ expectedly induced a red-shift in the absorption peak (from 757 to 790 nm in pH 6.5 buffer) compared to $Croc_{770}$ (Figure S3a and b). Croc is a hydrophobic dye, and its poor aqueous solubility is a major obstacle that appeared in the establishment of a new biomedical application. PEG−PLGA is a widely used FDA-approved copolymeric drug-delivery vehicle. Therefore, we used PEG−PLGA to encapsulate Croc to improve its biocompatibility, and it was fabricated by emulsion−solvent evaporation.[46,47] The loading parameters and physicochemical properties of nontargeted Cys−PEG−PLGA/$Croc_{770}$ (CPC_{770}) NPs, Cys−PEG−PLGA/$Croc_{815}$ (CPC_{815}) NPs, and targeted iRGD−PEG−PLGA/$Croc_{815}$ (PPC_{815}) NPs were characterized and are summarized in Table 1. Fourier transform infrared (FT-IR) spectroscopy was used to confirm the functional groups in Croc and PPC_{815}.[50] The peak at 1550 cm^{-1} is ascribed to the N=O stretch of the two nitro groups at $Croc_{815}$ (Figure S4a). As presented in Figure S4b, the intense peaks from 1098 to 1186 cm^{-1} are ascribed to the ether and ester groups of PEG and PLGA, respectively. The peak at 1601 cm^{-1} corresponds to the aromatic groups of Croc. The distinct peak at 1757 cm^{-1} refers to the C=O groups of Mal−PEG−PLGA. The larger, broad peak at 3448 cm^{-1} refers to the amine group and the amide bond of iRGD. The mean sizes of CPC_{770}, CPC_{815}, and PPC_{815} NPs were 182.3 ± 3.0, 183.3 ± 2.1, and 185.1 ± 3.3 nm, respectively, with a narrow distribution determined by DLS, indicating that conjugation with the iRGD peptide slightly increased the size of the NPs. The morphology and size of the PPC_{815} NPs were further proved by TEM. Figure 2a shows that the round-shaped PPC_{815} NPs were well-dispersed in aqueous solution. It shows

a mean size of 135.1 ± 0.5 nm (Figure 2b), which is smaller compared to the DLS measurements due to the hydrated conditions. The zeta potentials of CPC_{770}, CPC_{815}, and PPC_{815} NPs were −24.2 ± 2.1, −21.2 ± 1.4, and 1.2 ± 0.7, respectively. The more negative charges of CPC_{770} and CPC_{815} NPs were the result of terminal carboxylate groups on the PLGA shell. The significant increase of zeta potential of PPC_{815} NPs indicates successful attachment of the iRGD peptide on the NPs surface. The drug loadings (DL%) of PPC_{815} and CPC_{770} NPs estimated via HPLC-MS were 19.8 and 20.2%, respectively. The EE% of PPC_{815} and CPC_{770} NPs were 40.4 and 43.4%, respectively. The DL% and EE% of PPC_{815} and CPC_{770} NPs exhibited no obvious differences, indicating that the encapsulation ratio and the loading efficacy were not influenced by slight modification of the dye structure. The optical properties of the PPC_{815} NPs were measured in PBS buffers of different pH values. The absorption of PPC_{815} NPs exhibited a broad peak centered at 815 nm in pH 6.5 buffer solution, presenting a 25 nm red shift (from 790 to 815 nm) compared to that of free $Croc_{815}$ (Figure 2c). The red-shift is attributed to the J-type aggregates formed by head−tail molecular stacking that theoretically induces the appearance of lower-energy absorption bands. A similar observation was exploited in previous studies.[23] The optical properties of the free $Croc_{770}$ and CPC_{770} NPs were measured at different pH PBS buffers (Figure S3b and S5c). The absorption of CPC_{770} NPs exhibited a broad peak centered at 770 nm in pH 6.5 buffer solution, where the maximum was red-shifted by 13 nm compared to free that of $Croc_{770}$ (757 nm), which still maintained a pH-responsive optical property (Figure S5c and d). The different shiftings of the absorbance wavelengths for the two NPs are useful because the well-separated absorption maxima are exploited to deconvolute the optical signals. The absorbance peak ascended at 815 nm with the decrease of pH from pH 7.4 to 5.8 (similar to the pH value *in vivo*). Clearly, referring to the pH-responsive UV spectra of PPC_{815} NPs, we could feasibly differentiate the normal physiological conditions (pH 7.4) from a pathological tumor site (pH 6.0−7.0). Furthermore, it was found that PPC_{815} NPs would partially degrade in acidic conditions, as TEM images showed that the morphology of PPC_{815} became less consistent (Figure S6a and b); however, the shape of PPC NPs exhibits negligible change in physiological conditions (Figure S6c and d). As a result, the degradation in acidic medium is slow and mild and does not significantly hamper the desired drug-delivery purposes; we therefore propose that the NPs demonstrated excellent stability overall in different media over 24 h (Figure S7a). PPC_{815} NPs showed negligible change in particle size incubated under physiological condition over 1 week (Table S2), indicating their high biostability in different pH buffers and revealing suitable long-term biocompatibilities and bioactivities of NPs. DLS and polydispersity index (PDI) measurements also showed the mild increase of particle size, which demonstrated the degradation of the PPC_{815} NPs under acidic condition (Table S3). In Figure S7b, the change of photothermal effects
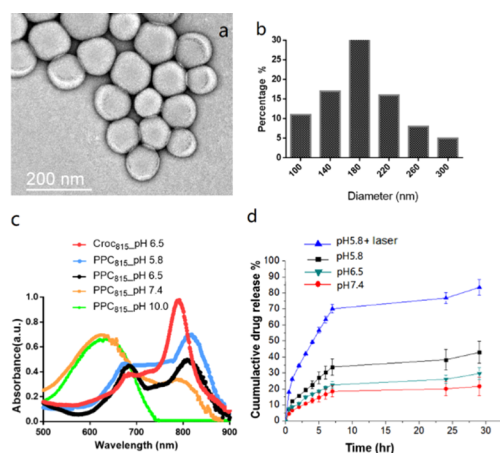

Figure 2. Characterization of PPC_{815} NPs. (a) TEM image and (b) size distribution of NPs. (c) UV absorption of $Croc_{815}$ and PPC_{815} NPs (50 μg/mL) at various pH values (10 mM PBS buffer). (d) Release profiles of $Croc_{815}$ from PPC_{815} NPs at various pH values with on/off laser irradiation of 1.0 W/cm^2 for 5 min.
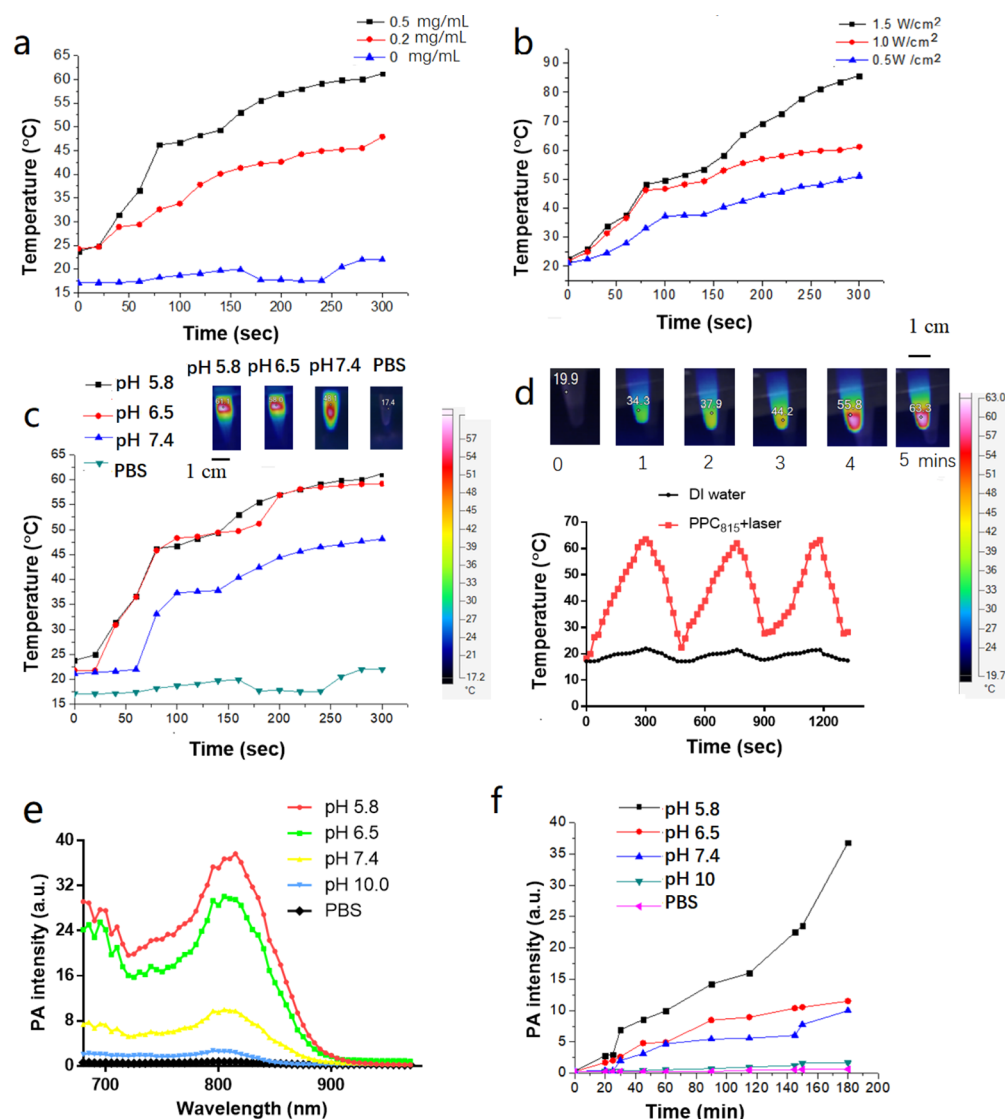
Figure 3. (a) Temperature elevation curves of PPC$_{815}$ NPs in different concentrations. (b) Temperature elevation curves of PPC$_{815}$ NPs in 50 μg/mL under different laser powers. (c) IR thermal images and temperature changes of PPC$_{815}$ NPs under different pH values under the 808 nm laser (1.0 W/cm², 5 min). (d) Multiple heating cycles of PPC$_{815}$ (50 μg/mL) upon three on/off repeated cycles (808 nm, 1.0 W/cm²). (e) Representative PA spectra of PPC$_{815}$ (50 μg/mL) under different pH buffer solutions in 180 min. (f) PA signal intensity of PPC$_{815}$ (50 μg/mL) versus a function of time under different buffers.

of PPC$_{815}$ NPs could be readily observed in adjusting the NIR laser on or off three times after a 24 h incubation in buffer media. This indicates that the PPC$_{815}$ NPs have a stable heating generation and a high heat conversion rate.

3.2. NIR-Stimulated Release of Croc$_{815}$ from PPC$_{815}$ NPs. PPC$_{815}$ NPs were selected as a model to determine the Croc$_{815}$ release from the nanoparticles form in vitro. The release kinetics of PPC$_{815}$ NPs was controlled with NIR laser irradiation (0.5, 1.0, and 1.5 W/cm²) and manipulation of pH (pH 5.8, 6.5, and 7.4) at 37 °C. Upon different power pulsing irradiations, the drug-release profile revealed a power density-dependent behavior (Figure S8a). When a laser intensity of 1.0 W/cm² was selected to evaluate the drug-release profile under different pH buffers (Figure 2d), a small portion (20%) of Croc$_{815}$ was released from NPs in pH 7.4 buffer within 30 h. However, ~40% of the trapped Croc was released from NPs in pH 5.8 without laser irradiation within 30 h. The higher release rate of NPs in acidic condition referred to the faster degradation rate of PLGA in a mildly acidic tumor environ-

ment, which is similar to the tumor microenvironment. Moreover, NPs showed a faster and higher (80%) release from NPs in pH 5.8 buffer under laser irradiation. Enhanced Croc$_{815}$ release was attributed to the heat energy from the NIR dye Croc$_{815}$ upon NIR laser, which resulted in hyperthermia-induced collapse of the NPs. The release profiles of Croc$_{815}$ from PPC$_{815}$ NPs without laser irradiation were also studied under storage conditions (at 4 °C and dark) and physiological condition (pH 7.4 PBS at 37 °C) for 10 days. As shown in Figure S8b, the leakage of Croc$_{815}$ from PPC$_{815}$ is <20% even after 10 days, which is mildly lower than that of the PLGA-based delivery system.[51] The higher stability of these formulations provides evidence of the attachment PEG coating barrier on the PLGA NPs. The result suggests that PPC$_{815}$ NPs have a high potential for drug-delivery applications.

3.3. Photothermal Ability of PPC$_{815}$ NPs. To explore the feasibility of PPC$_{815}$ NPs as a photothermal agent, photo-thermal-heating curves of PPC$_{815}$ NPs and corresponding thermal images were monitored and recorded. Figure 3a shows
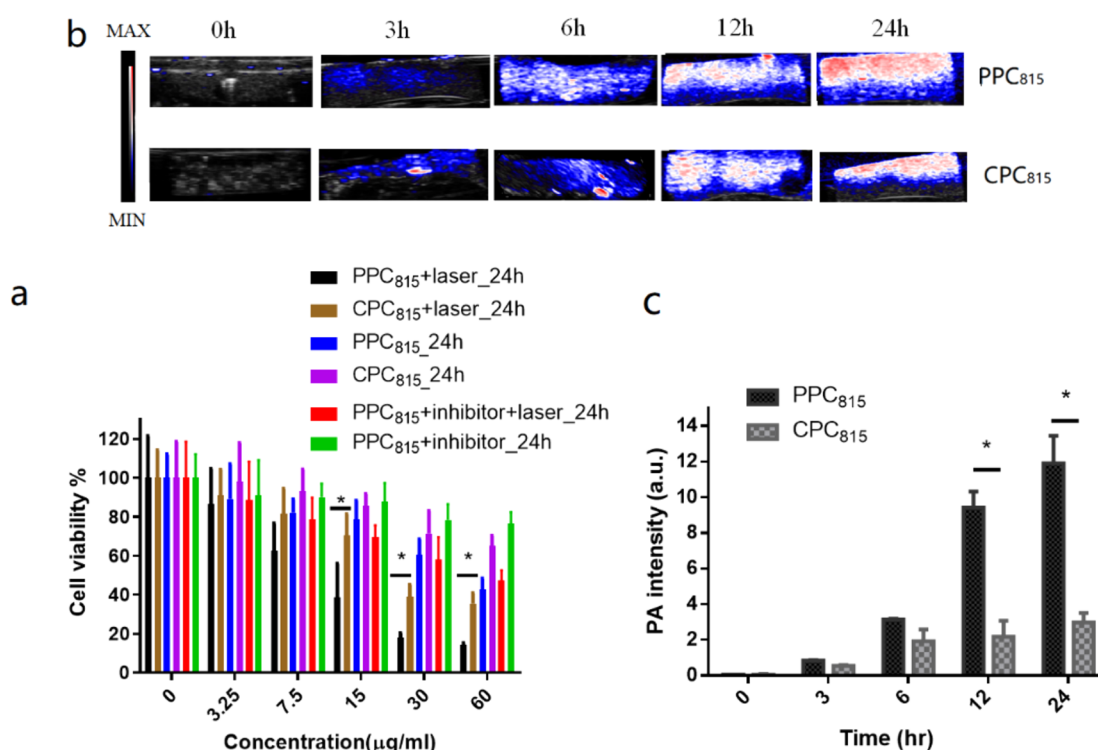
Figure 4. (a) Cell viability of MDA-MB-231 cells treated with different concentrations of PPC_{815} with and without preincubation of 10 μL of 10 mM iRGD inhibitor and CPC_{815} (nontargeted) with and without laser irradiation (n = 5) after a 24 h incubation. (b) PA signal of each phantom consisting of MDA-MB-231 with 50 μg/mL PPC_{815} (targeted) and CPC_{815} (nontargeted) for different time points. (c) Quantitative measurements at 815 nm at different time points. $p < 0.05$.

that the temperature of PPC_{815} NPs increased with concentration under 808 nm laser irradiation (1.0 W/cm^2). On the contrary, the temperature of pure PBS showed negligible changes, which revealed that the NPs could convert NIR light into thermal energy efficiently. Clearly, PPC_{815} NPs are positively proportional to the laser power density in photothermal-conversion efficiency (Figure 3b). Moreover, the temperature elevation of PPC_{815} NPs was enhanced in a pH-dependent aqueous solution upon 808 nm laser irradiation (1.0 W/cm^2) (Figure 3c). The temperature elevation of PPC_{815} NPs (50 μg/mL) was significantly increased from 24.5 to 62.3 °C in pH 5.8 and to 58.1 °C in pH 6.5, which was higher than that for the equivalent amount of NPs in pH 7.4 (46.1 °C). The photothermal stability of PPC_{815} NPs was investigated by applying triple recycling temperature variations of PPC_{815} NPs solution, and no significant deterioration of the recycling was seen (Figure 3d), revealing the great potential of PPC_{815} NPs as a PTT agent to treat cancer *in vivo*. The photothermal conversion efficiencies (η) of PPC_{815} and CPC_{770} NPs were calculated to be 34.7% and 32.0%, respectively, in pH 6.5 buffer solution. These results showed that PPC_{815} and CPC_{770} NPs have intense photothermal conversion ability, and they lay a firm foundation to be applied in preclinical usage.

3.4. Photoacoustic Imaging in Tube Phantom. Before using PA for *in vivo* tumor detection, the changes in PA signals of PPC_{815} in pH buffer solutions from pH 7.4 to 5.8 were investigated by absorption studies.

The full PA spectra of PPC_{815} is shown in Figure 3e. The PA signals of PPC_{815} were barely detectable at pH 7.4 or alkaline condition. Interestingly, we revealed that the PA signal's intensity was enhanced with the decrease of pH and increased

gradually over time (Figure 3f). At pH 5.8, PPC_{815} NPs revealed a prominent PA signal enhancement upon a testing period of 3 h. In comparison, the PPC_{815} NPs at pH 7.4 exhibited a negligible signal change across time. Therefore, the PA signals of PPC_{815} NPs at pH 5.8 were 4.0-fold higher than that of PPC_{815} NPs tested at pH 7.4 upon a 3 h incubation. Quantity analysis of the PPC_{815} NPs at different pH buffers revealed that PA exhibited pH sensing along different time points in PE tubes and 1% agarose gel phantom. This indicates that PPC_{815} NPs show promising properties as a PA contrast agent in its "activated" stage when in TME, as also shown in Figure S9.

3.5. Cytotoxicity and Photothermal Therapy of CPC_{815} and PPC_{815} NPs *In Vitro*. Low toxicity plays important roles in the design of any nanotherapeutic agent for biological imaging and tumor inhibition. The determination of the *in vitro* cytotoxicities of CPC_{815} and PPC_{815} NPs with and without laser irradiation against breast cancer cells was carried out by CCK-8 assay in triplicate. As presented in Figure 4a, without laser irradiation, the IC_{50} values (i.e., the drug concentrations required to induce 50% cell death within a certain period) of CPC_{815} and PPC_{815} NPs were 75.7 and 60.2 μg/mL after a 24 h incubation, respectively. Compared to the IC_{50} of free $Croc_{815}$ (110.1 μg/mL) (Figure S10), the cell viabilities of PPC_{815} or CPC_{815} significantly decreased, revealing that the encapsulation of $Croc_{815}$ resulted in higher cytotoxicity of the $Croc_{815}$ dye. Upon NIR laser irradiation (1.0 W/cm^2, 5 min), the IC_{50} values of CPC_{815} and PPC_{815} significantly decreased to 27.8 and 11.2 μg/mL, respectively, demonstrating the efficient photothermal therapeutic effect *in vitro*. Furthermore, the cell viability after being treated with PPC_{815} appeared to be relatively lower than that of CPC_{815}
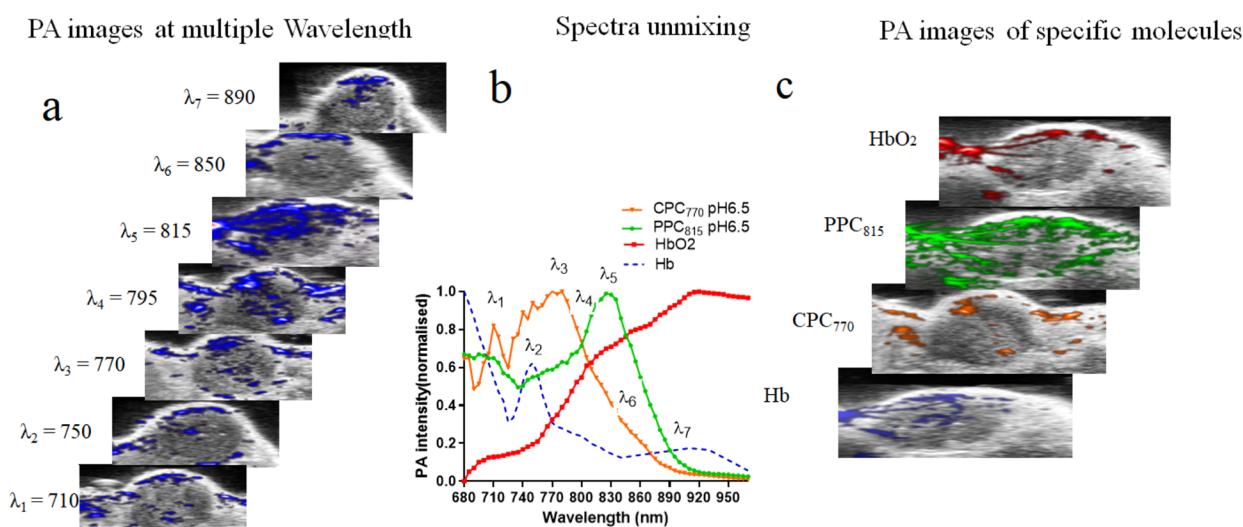
Figure 5. Multiplexed PA tomography. (a) PA images acquired at multiple wavelengths. (b) PA spectra unmixing of CPC_{770} and PPC_{815} NPs in pH 6.5 buffer solution with oxygenated hemoglobin (OxH, red) and deoxygenated hemoglobin (deOxH, blue). (c) Multiplexed PA images of CPC_{770}, PPC_{815} NPs, OxH, and deOxH within tumors when overlaid with ultrasound images.
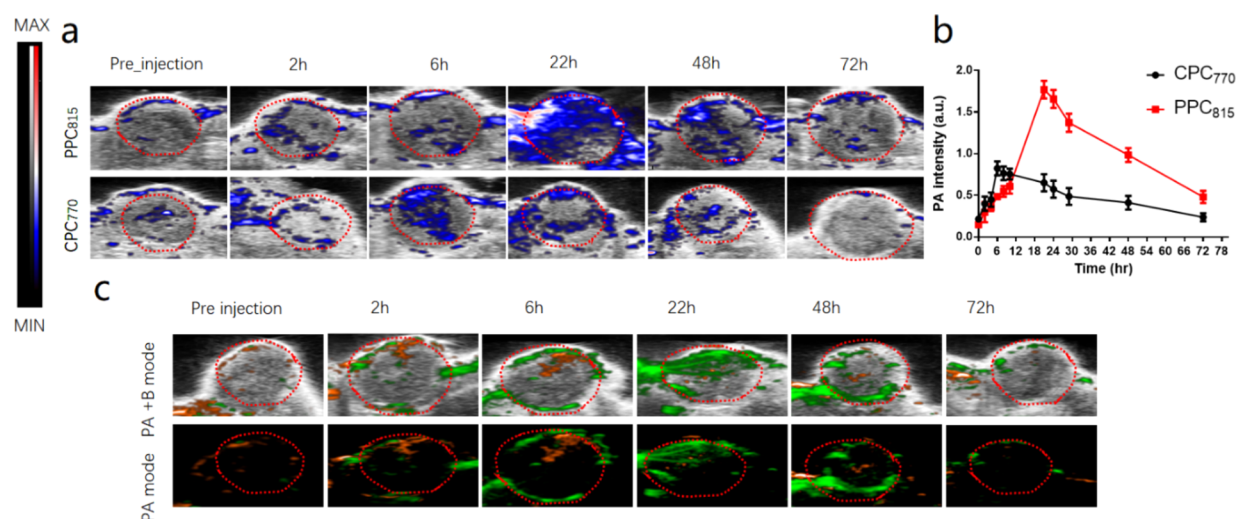

Figure 6. (a) Monitoring of NPs accumulation with PA imaging. Heat map of PA-US overlay images of PPC_{815} and CPC_{770} NPs (1:1 w/w, 5 mg/kg per each NP, 200 μL) injected into the mice bearing MDA-MB-231 ductal carcinoma in situ after 0, 2, 6, 22, 48, and 72 h of NP accumulation in tumors. (b) Average PA signal intensity at 815 nm of PPC_{815} NPs and 770 nm of CPC_{770} NPs within tumors along different time points ($n = 5$). (c) Multiplexed in vivo tumor PA images of CPC_{770} and PPC_{815} NPs with accumulation at the same single mouse over the postinjection time. Heat map of PA-US overlay images after intravascular injection of CPC_{770} NPs (orange) and PPC_{815} NPs (green).

during the testing concentration, which could be attributed to the improved targeting efficiency of NPs in MDA-MB-231 cancer cells brought about by iRGD conjugated on the surface of NPs. To test the iRGD targeting properties, a block experiment using free iRGD as an inhibitor was performed in the cell viability test. Before addition of PPC_{815} NPs, 10 μL of 10 mM iRGD was preincubation into the cell and for 3 h, according to the same procedure as previously mentioned. The competing group (PPC_{815} + inhibitor + laser) exhibited much lower cytotoxicity compared to the group of PPC_{815} + laser. It revealed that the iRGD preincubation appeared to block all the surface receptors for binding with the PPC_{815}. The result is consistent with Figure 4a, confirming the targeting ability of the PPC_{815} NPs between iRGD and the $a_v\beta_3$ receptor, which is similar to our previously published work.[28]

3.6. Photoacoustic Imaging of NPs in Cell Phantom.
To test the image contrast of the NPs, in vitro PA monitoring

was measured using agarose gel phantom merged with $\alpha_v\beta_3$ integrin-overexpressed cancer cell MDA-MB-231 incubated with 50 $\mu g/mL$ of PPC_{815} (targeting) and CPC_{815} (non-targeting) NPs for different time periods (0, 3, 6, 12, and 24 h postinjection). The PA imaging remained strong within 24 h (Figure 4b and c). This indicated that the PA signal at 815 nm was very weak in the cells at the beginning of the measurement, and then the signal intensity increased with the incubation time. Compared to the CPC_{815} NPs signals, PPC_{815} rapidly increased along time. For instance, the PA signal intensity of PPC_{815} was approximated to be 4.5 times stronger than that of CPC_{815} after a 12 h incubation, demonstrating that the cellular uptake of PPC_{815} was significant increased due to the selective accumulation to the $\alpha_v\beta_3$ integrin receptor that is overexpressed on the cancer cells.

3.7. In Vivo Multispectral Unmixing of PA Imaging.
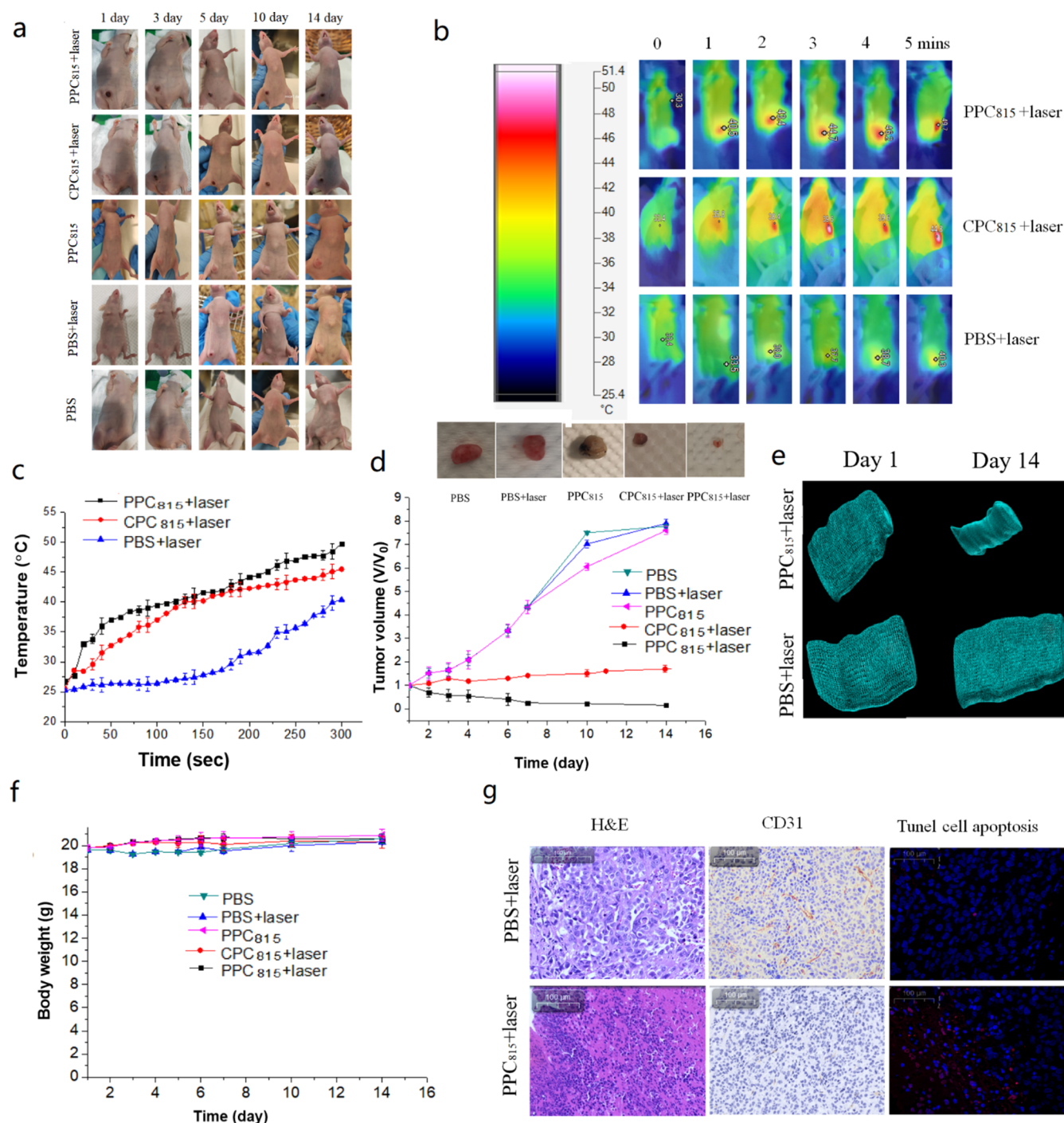The PA images at different wavelengths (710, 750, 770, 795,

Figure 7. *In vivo* photothermal therapy of the MDA-MB-231 tumor-bearing mice after injection of PBS, CPC$_{815}$, and PPC$_{815}$ with laser irradiation after 24 h of injection (5 mg/kg, 1.5 W/cm^2). (a) Photographs of the tumor across 14 days after 5 min of 1.5 W/cm^2 NIR irradiation. (b) Thermal images and (c) corresponding temperature changes of tumor site after 24 h postinjection. (d) Relative tumor-growth curve. The inset is the photographs of relevant tumors that originated from each group in (d). (e) 3D volume of the tumor before and after treatment. (f) Body weight after various treatments indicated in 14 days. (g) H&E staining of tumor tissues after 14 days of PTT treatment as indicated, immunohistochemical analysis of the expressions of CD31 in tumor tissues of mice, and TUNEL staining for apoptosis in tumor sections; scale bar represents 100 μm.

815, 850, and 890 nm) are used to unmix different kinds of contrast agents, based on unique PA spectral signatures. The formation of targeted PPC$_{815}$ and nontargeted CPC$_{770}$ NPs that can be readily exploited to deconvolute each other with high signal-to-noise ratios enables powerful application of multiplexed PA imaging of a specific chromophore composition, with high potential according to the distinct absorbance spectra of targeted PPC$_{815}$ and nontargeted CPC$_{770}$ NPs. The

PA instrument is capable of recording multispectral imaging as shown in Figure 5. The PA responses of tumors were collected with sequential images of the tumor at multiple wavelengths, and image reconstruction was performed with the acquired data (Figure 5a). The result in Figure 5b shows the PA spectra of PPC$_{815}$ and CPC$_{770}$ at pH 6.5. The signals from targeted PPC$_{815}$ and nontargeted CPC$_{770}$ can be distinguished via PA multispectral scanning with distinct absorbance maxima at 770

and 815 nm, which assisted the deconvolution from endogenous signals (Figure 5b). PA images of NPs, OxH, and deOxH can be recorded in real time and overlaid with ultrasound images as shown in Figure 5c.

3.8. *In Vivo* Distribution of PPC$_{815}$ NPs and CPC$_{770}$ by PA Imaging. Notably, we studied the targeting effect of $\alpha_v\beta_3$ integrin-positive tumor on the accumulation levels and pharmacokinetic profiles of CPC$_{770}$ and PPC$_{815}$ NPs in tumor over time in MDA-MB-231 tumor-bearing nude mice using PA imaging. Briefly, PPC$_{815}$ (targeting) and CPC$_{770}$ NPs (nontargeting) (1:1, 5 mg/kg, 200 μL) were intravenously coinjected in tumor-bearing mice, and PA images were acquired at seven different wavelengths at 0, 2, 4, 6, 8, 12, 24, 36, 48, and 72 h (Figure 6a). The accumulations and spatial distributions of the NPs were multiplexed from endogenous PA signals. The results are depicted in Figure 6b. The PA signal of PPC$_{815}$ NPs increased quickly, peaking at 22 h, and started to decrease thereafter. A weak signal remained even after 72 h postinjection, indicating a longer circulation time. When overlaid with ultrasound images of the tumor, the PPC$_{815}$ NP signals can be visualized separately into the deep tissue with high resolution at the tumor site after 22 h postinjection. However, for nontargeting CPC$_{770}$ NPs, the PA signal gradually increased until reaching its highest level at 6 h postinjection, with relatively low retention in the tumor afterward. The average PA intensity indicated a slight increase in the PA signal after intravenous injection of CPC$_{770}$ NPs, and thus, no obvious accumulation can be observed within the tumor. Moreover, the CPC$_{770}$ NPs PA signal has a relatively high retention around the periphery of the tumor. To compare the results of CPC$_{770}$ NPs and the control (nontargeted CPC$_{815}$ NPs), both were injected into tumor-bearing mice and their PA intensities were recorded (Figure S11). The PA signal intensity of CPC$_{815}$ within the tumor also reached the peak level at 6 h postinjection, then started to decrease, and finally returned to the level similar to that before injection, exhibiting a similar trend change of the PA signal of CPC$_{770}$ NPs. At each given time point, the targeted PPC$_{815}$ NPs revealed a significantly greater PA signal intensity compared to CPC$_{770}$ NPs (Figure 6b). The PPC$_{815}$ NPs achieved a 2.8 times PA signal enhancement compared to CPC$_{770}$ NPs at 22 h. This systematic accumulation of PPC$_{815}$ NPs reveals the preferred targeting of the $\alpha_v\beta_3$ integrin, which is overexpressed in many types of tumor neovasculature and therefore selectively targets the acidic extracellular microenvironment (pH 6.5−6.8) in tumor tissues.[31] Quantitative PA results showed that iRGD-targeting PPC$_{815}$ NPs accumulated in tumor longer than nontargeting CPC$_{770}$ NPs. In particular, the molecular structure of Croc$_{815}$ and the targeting effect resulted in PPC$_{815}$ NPs generating a significant increase in PA signal as compared to CPC$_{770}$.

The heat map of the PA signal only provided a one-frame tumor image at a time point, whereas multiplexed PA images can be obtained through the unmixing algorithm via Vevo Analysis Software and thus reflect the total information of the target site. The result is to track the optoacoustic signal change corresponding to the active chromophores to study their pharmacokinetics. PA signals between PPC$_{815}$ and CPC$_{770}$ can be separated due to each unique maximum between two dyes spectrally and the bare low signal of CPC$_{770}$ at higher wavelengths (840 nm). Multiplexed *in vivo* tumor PA images and PA-US overlay images of CPC$_{770}$ and PPC$_{815}$ NPs accumulation in the same single mouse versus the post-

injection time are shown in Figure 6c. The PA signal intensity and time-dependent signal changes are similar to the results shown in Figure 6a. The ability to simultaneously image both targeting and nontargeting nanoprobes PA signal would improve the reliability by reducing experimental variability. Furthermore, this ability offers insight into the involvement of the tissue-targeting property in various aspects such as pharmacokinetic profile and selective tissue-binding affinity. Therefore, the utilization of distinct absorbance characteristics with different surface modifications in NPs provides a capacity for synchronously screening and investigating tumor properties.

3.9. *In Vivo* Antitumor Efficacy of PPC$_{815}$ NPs. With the encouraging results from *in vitro* PA imaging and the capability in demolishing malignant cancer cells with high photothermal conversion efficiencies of CPC$_{815}$ and PPC$_{815}$, we next examined the *in vivo* photothermal antitumor effect. Figure 7a shows the photographs of the MDA-MB-231 tumor-bearing mice injected with PBS, CPC$_{815}$, PPC$_{815}$, CPC$_{815}$ + laser, and PPC$_{815}$ + laser (5 mg/kg, 100 μL) at different time intervals. Mice receiving intravenous injection of PPC$_{815}$ NPs coupled with laser irradiation exhibited a significant tumor regression when compared with other groups, thus indicating the *in vivo* photothermal tumor inhibition effect. The change of corresponding temperatures in the tumor tissue followed by laser irradiation is depicted in Figure 7b and c. Moreover, the data revealed that the PBS + laser group resulted in a slight temperature elevation and reached ∼38 °C. However, the groups that received PPC$_{815}$ + laser or CPC$_{815}$ NPs + laser resulted in a substantial temperature elevation to 49 °C, which reaches the damage threshold for irreversible injury. The change of relative tumor volumes was recorded and is plotted in Figure 7d. The prominent PTT-augmented therapeutic outcome with PPC$_{815}$ NPs coupled with laser irradiation was attributed and triggered by the active pH-sensitive targeting property within TME, which results in desirable photothermal ablation. Moreover, the temperature of the surrounding healthy tissues at the opposite side of the tumor region slightly increased to ∼38 °C after laser irradiation, which could not induce obvious organ damage or inflammatory lesions in these normal sites. These results demonstrated that the polymeric NPs, under laser irradiation, have relatively little adverse effects on normal tissues, making PPC$_{815}$ NPs a novel and safe nanomedicine for cancer theranostics (Figure S12). In the absence of a targeting effect, the CPC$_{815}$ coupled with laser irradiation only exhibited the minimal tumor-inhibition efficacy. PPC$_{815}$ without PTT revealed in a low tumor-inhibition effect, very similar to that of the laser-only group, while the laser-only group exhibited negligible suppression on tumors. The 3D volume rendering of PA images for PPC$_{815}$ and PBS before and after laser treatment were recorded to determine the accurate size of the tumor (Figure 7e). The pre- and postinjection volume sizes of the tumor are 50 and 23.5 mm^3, respectively, which are smaller than that of control group (153 mm^3). The anticancer effect of PTT was confirmed by H&E, CD31, and TUNEL assay (Figure 7g). H&E-stained tumors in PBS + laser did not induce significant damage, whereas PPC$_{815}$ + laser treatment resulted in tumor shrinkage and necrosis. The immunohistochemical assay with CD31 detected immunoreactivity in the PBS + laser group that indicated the formation of blood vessels. In contrast, immunoreactivity is significantly reduced in the PPC$_{815}$ + laser treatment group. The TUNEL staining in the PBS + laser
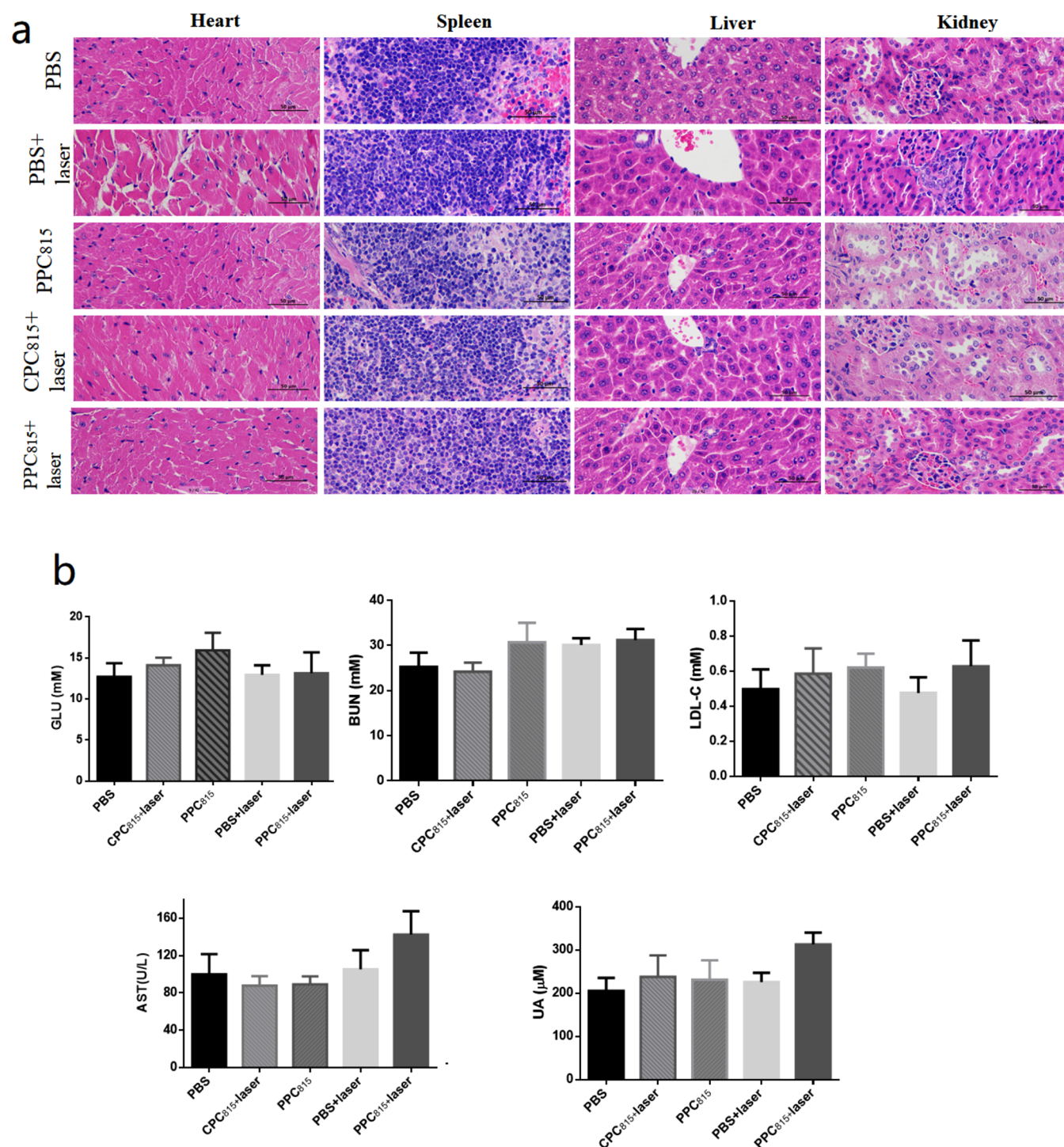
Figure 8. (a) H&E stained organs of different treatment groups that were acquired at 14 days. No noticeable changes were observed in these organs; scale bar is 50 μm. (b) Blood biochemical indexes of blood glucose (GLU), blood urea nitrogen (BUN), low-density lipoprotein cholesterol (LDL-C), aspartate aminotransferase (AST), and high-plasma uric acid (UA) that were acquired at 14 days.

group revealed a small number of apoptotic cells, whereas PPC_{815} + laser treatment induced apparent apoptotic cells.

Our histopathological analysis proved that the PTT treatment, coupled with iRGD-targeted PPC_{815} NPs, inhibited tumor proliferation. Furthermore, the nanoprobe-treated nude mice showed no obvious change in their body weights for 14 days, revealing that no obvious effects originated from the NPs nor laser irradiation (Figure 7f). To investigate the potential toxicity after intravenous injection of nontargeted CPC_{770},

CPC_{815}, and iRGD-targeting PPC_{815} NPs, organs from tumor-bearing mice were subjected to H&E analysis (Figure 8). The change of body weight of each mouse was recorded. Moreover, the blood biochemical indexes were investigated. No observable abnormalities in the laser and NPs treatment group indicated that the laser and NPs possess no toxicity to main organs (Figure 8a). The blood chemical indexes including alanine aminotransferase (ALT), aspartate aminotransferase (AST), blood urea nitrogen (BUN), plasma uric

acid (UA), blood glucose (GLU), and low-density lipoprotein cholesterol (LDL-C) levels were measured and revealed no obvious acute toxicity.

4. CONCLUSIONS

In summary, we developed pH-sensitive chromophores Croc$_{770}$ and Croc$_{815}$ followed by encapsulation with Mal−PEG−PLGA copolymer with surface modification to obtain nontargeting CPC$_{770}$ NPs and iRGD-targeting PPC$_{815}$ NPs for PTT treatment and *in vivo* multiplexed PA imaging. The photo-acoustic efficiencies of CPC$_{770}$ and PPC$_{815}$ NPs are considerably greater than the hemoglobin species in blood, which allows clear separation of the PA signal for determining the distribution of NPs inside the tumor within the same animal after administration. The mice injected with targeted PPC$_{815}$ NPs showed great PA signal enhancement in the tumor as compared to the CPC$_{770}$ NPs during the investigation. The PPC$_{815}$ NPs also demonstrated an ability to effectively inhibit tumor growth. Preliminary toxicity analysis revealed no apparent acute toxicity to major organs after a single dose of intravenously injected PPC$_{815}$ NPs. Our novel nanoplatform lays the foundation of a PA theranostic, which simultaneously provides quantifiable diagnosis as well as monitoring of the PTT therapeutics outcome. This dual-role approach enlightens the development of tumor diagnosis with multiplexed PA-based theranostic nanoplatforms and expands the direction of next-generation novel PA theranostics in the fields of biology and medicine.

■ ASSOCIATED CONTENT

Ⓢ Supporting Information

The Supporting Information is available free of charge at https://pubs.acs.org/doi/10.1021/acsabm.0c01578.

Experimental details for blood analysis and TUNEL assay, data and figures including synthetic scheme for Crco$_{815}$ and Croc$_{770}$, ^{1}H NMR spectra and mass spectra of Croc$_{815}$ and Croc$_{770}$ dyes, UV/vis absorption plots of Croc$_{815}$ and Croc$_{770}$ dyes, temperature change profiles of Croc$_{815}$ and Croc$_{770}$, characterization of CPC$_{770}$ NPs, stability test for PPC$_{815}$, release profile of Croc$_{815}$ from PPC$_{815}$ upon different conditions, detailed calculation of encapsulation efficiency, drug loading, and photothermal conversion efficiency of NPs, and *in vitro* and *in vivo* PA characterization for NPs (PDF)

■ AUTHOR INFORMATION

Corresponding Authors

Yan-Juan Gu − *Department of Applied Biology and Chemical Technology, The Hong Kong Polytechnic University, Hung Hom, Hong Kong, China*; Email: yanjuan.gu@polyu.edu.hk

Wing-Tak Wong − *Department of Applied Biology and Chemical Technology, The Hong Kong Polytechnic University, Hung Hom, Hong Kong, China*; Ⓞ orcid.org/0000-0001-9222-8376; Email: w.t.wong@polyu.edu.hk

Authors

Shiying Li − *Department of Applied Biology and Chemical Technology, The Hong Kong Polytechnic University, Hung Hom, Hong Kong, China*

Kwok-Ho Lui − *Department of Applied Biology and Chemical Technology, The Hong Kong Polytechnic University, Hung Hom, Hong Kong, China*

Xin Li − *Department of Applied Biology and Chemical Technology, The Hong Kong Polytechnic University, Hung Hom, Hong Kong, China*

Xueyang Fang − *Department of Applied Biology and Chemical Technology, The Hong Kong Polytechnic University, Hung Hom, Hong Kong, China*

Wai-Sum Lo − *Department of Applied Biology and Chemical Technology, The Hong Kong Polytechnic University, Hung Hom, Hong Kong, China*

Complete contact information is available at:
https://pubs.acs.org/10.1021/acsabm.0c01578

Author Contributions

[†]S.L. and K.-H.L. contributed equally.

■ ACKNOWLEDGMENTS

■ ABBREVIATIONS

NIR, near-infrared
(Croc), croconaine dyes
NPs, nanoparticles; tumor microenvironment
PLGA, poly(lactic acid/glycolic acid)
PEG, poly(ethylene glycol)
Mal−PEG−PLGA−COOH, maleimide−poly(ethylene glycol)−poly(lactide-*co*-glycolide)−COOH
CPC$_{815}$, Cys−PEG−PLGA/Croc$_{815}$
CPC$_{770}$, Cys−PEG−PLGA/Croc$_{770}$
PPC$_{815}$, iRGD−PEG−PLGA/Croc$_{815}$
TEM, transmission electron microscope
DLS, dynamic light scattering
PBS, phosphate buffer solution
H&E, hematoxylin and eosin
OxH, oxygenated hemoglobin
deOxH, deoxygenated hemoglobin
ROI, region of interest
ALT, alanine aminotransferase
AST, aspartate aminotransferase
BUN, blood urea nitrogen
UA, plasma uric acid
GLU, blood glucose
LDL-C, low-density lipoprotein cholesterol

■ REFERENCES

(1) Li, S.; Deng, Q.; Zhang, Y.; Li, X.; Wen, G.; Cui, X.; Wan, Y.; Huang, Y.; Chen, J.; Liu, Z.; Wang, L.; Lee, C. Rational Design of Conjugated Small Molecules for Superior Photothermal Theranostics in the NIR-II Biowindow. *Adv. Mater.* **2020**, 32 (33), 2001146.
(2) Xiao, Y.; Xiang, C.; Li, S.; Mao, C.; Chen, H.; Chen, J.; Tian, S.; Cui, X.; Wan, Y.; Huang, Z.; Li, X.; Zhang, X.; Guo, W.; Lee, C.

Single-Photomolecular Nanotheranostics for Synergetic Near-Infrared Fluorescence and Photoacoustic Imaging-Guided Highly Effective Photothermal Ablation. *Small* **2020**, *16* (34), 2002672.

(3) Zhen, X.; Zhang, J.; Huang, J.; Xie, C.; Miao, Q.; Pu, K. Macrotheranostic Probe with Disease-Activated Near-Infrared Fluorescence, Photoacoustic, and Photothermal Signals for Imaging-Guided Therapy. *Angew. Chem., Int. Ed.* **2018**, *57* (26), 7804−7808.

(4) Kim, C.; Favazza, C.; Wang, L. V. In Vivo Photoacoustic Tomography of Chemicals: High-Resolution Functional and Molecular Optical Imaging at New Depths. *Chem. Rev.* **2010**, *110* (5), 2756−2782.

(5) Wang, L. V.; Hu, S. Photoacoustic Tomography: In Vivo Imaging from Organelles to Organs. *Science (Washington, DC, U. S.)* **2012**, *335* (6075), 1458−1462.

(6) Upputuri, P. K.; Pramanik, M. Recent Advances toward Preclinical and Clinical Translation of Photoacoustic Tomography: A Review. *J. Biomed. Opt.* **2017**, *22* (4), 041006.

(7) Nie, L.; Chen, X. Structural and Functional Photoacoustic Molecular Tomography Aided by Emerging Contrast Agents. *Chem. Soc. Rev.* **2014**, *43* (20), 7132−7170.

(8) Weber, J.; Beard, P. C.; Bohndiek, S. E. Contrast Agents for Molecular Photoacoustic Imaging. *Nat. Methods* **2016**, *13* (8), 639−650.

(9) Zeng, L.; Ma, G.; Lin, J.; Huang, P. Photoacoustic Probes for Molecular Detection: Recent Advances and Perspectives. *Small* **2018**, *14* (30), 1800782.

(10) Merkes, J. M.; Zhu, L.; Bahukhandi, S. B.; Rueping, M.; Kiessling, F.; Banala, S. Photoacoustic Imaging Probes Based on Tetrapyrroles and Related Compounds. *Int. J. Mol. Sci.* **2020**, *21* (9), 3082.

(11) Herzog, E.; Taruttis, A.; Beziere, N.; Lutich, A. A.; Razansky, D.; Ntziachristos, V. Optical Imaging of Cancer Heterogeneity with Multispectral Optoacoustic Tomography. *Radiology* **2012**, *263* (2), 461−468.

(12) Jacques, S. L. Optical Properties of Biological Tissues: A Review. *Phys. Med. Biol.* **2013**, *58* (11), R37−R61.

(13) Stritzker, J.; Kirscher, L.; Scadeng, M.; Deliolanis, N. C.; Morscher, S.; Symvoulidis, P.; Schaefer, K.; Zhang, Q.; Buckel, L.; Hess, M.; Donat, U.; Bradley, W. G.; Ntziachristos, V.; Szalay, A. A. Vaccinia Virus-Mediated Melanin Production Allows MR and Optoacoustic Deep Tissue Imaging and Laser-Induced Thermotherapy of Cancer. *Proc. Natl. Acad. Sci. U. S. A.* **2013**, *110* (9), 3316−3320.

(14) Ntziachristos, V.; Razansky, D. Molecular Imaging by Means of Multispectral Optoacoustic Tomography (MSOT). *Chem. Rev.* **2010**, *110* (5), 2783−2794.

(15) Taruttis, A.; Ntziachristos, V. Advances in Real-Time Multispectral Optoacoustic Imaging and Its Applications. *Nat. Photonics* **2015**, *9* (4), 219−227.

(16) Gujrati, V.; Mishra, A.; Ntziachristos, V. Molecular Imaging Probes for Multi-Spectral Optoacoustic Tomography. *Chem. Commun.* **2017**, *53* (34), 4653−4672.

(17) Deán-Ben, X. L.; Gottschalk, S.; Mc Larney, B.; Shoham, S.; Razansky, D. Advanced Optoacoustic Methods for Multiscale Imaging of in Vivo Dynamics. *Chem. Soc. Rev.* **2017**, *46* (8), 2158−2198.

(18) Razansky, D.; Buehler, A.; Ntziachristos, V. Volumetric Real-Time Multispectral Optoacoustic Tomography of Biomarkers. *Nat. Protoc.* **2011**, *6* (8), 1121−1129.

(19) Jo, J.; Lee, C. H.; Kopelman, R.; Wang, X. In Vivo Quantitative Imaging of Tumor PH by Nanosonophore Assisted Multispectral Photoacoustic Imaging. *Nat. Commun.* **2017**, *8* (1), 471.

(20) Yang, Z.; Song, J.; Tang, W.; Fan, W.; Dai, Y.; Shen, Z.; Lin, L.; Cheng, S.; Liu, Y.; Niu, G.; Rong, P.; Wang, W.; Chen, X. Stimuli-Responsive Nanotheranostics for Real-Time Monitoring Drug Release by Photoacoustic Imaging. *Theranostics* **2019**, *9* (2), 526−536.

(21) Cox, B.; Laufer, J. G.; Arridge, S. R.; Beard, P. C. Quantitative Spectroscopic Photoacoustic Imaging: A Review. *J. Biomed. Opt.* **2012**, *17* (6), 061202.

(22) Lu, H. D.; Wilson, B. K.; Lim, T. L.; Heinmiller, A.; Prud'homme, R. K. Real-Time and Multiplexed Photoacoustic Imaging of Internally Normalized Mixed-Targeted Nanoparticles. *ACS Biomater. Sci. Eng.* **2017**, *3* (3), 443−451.

(23) Lu, H. D.; Wilson, B. K.; Heinmiller, A.; Faenza, B.; Hejazi, S.; Prud'homme, R. K. Narrow Absorption NIR Wavelength Organic Nanoparticles Enable Multiplexed Photoacoustic Imaging. *ACS Appl. Mater. Interfaces* **2016**, *8* (23), 14379−14388.

(24) Bayer, C. L.; Chen, Y.-S.; Kim, S.; Mallidi, S.; Sokolov, K.; Emelianov, S. Multiplex Photoacoustic Molecular Imaging Using Targeted Silica-Coated Gold Nanorods. *Biomed. Opt. Express* **2011**, *2* (7), 1828.

(25) Li, P.-C.; Wang, C.-R. C.; Shieh, D.-B.; Wei, C.-W.; Liao, C.-K.; Poe, C.; Jhan, S.; Ding, A.-A.; Wu, Y.-N. In Vivo Photoacoustic Molecular Imaging with Simultaneous Multiple Selective Targeting Using Antibody-Conjugated Gold Nanorods. *Opt. Express* **2008**, *16* (23), 18605.

(26) Liu, C.; Li, S.; Gu, Y.; Xiong, H.; Wong, W.; Sun, L. Multispectral Photoacoustic Imaging of Tumor Protease Activity with a Gold Nanocage-Based Activatable Probe. *Mol. Imaging Biol.* **2018**, *20* (6), 919−929.

(27) Li, H.-J.; Du, J.-Z.; Du, X.-J.; Xu, C.-F.; Sun, C.-Y.; Wang, H.-X.; Cao, Z.-T.; Yang, X.-Z.; Zhu, Y.-H.; Nie, S.; Wang, J. Stimuli-Responsive Clustered Nanoparticles for Improved Tumor Penetration and Therapeutic Efficacy. *Proc. Natl. Acad. Sci. U. S. A.* **2016**, *113* (15), 4164−4169.

(28) Li, S.; Lui, K.-H.; Tsoi, T.-H.; Lo, W.-S.; Li, X.; Hu, X.; Chi-Shing Tai, W.; Hiu-Ling Hung, C.; Gu, Y.-J.; Wong, W.-T. PH-Responsive Targeted Gold Nanoparticles for in Vivo Photoacoustic Imaging of Tumor Microenvironments. *Nanoscale Adv.* **2019**, *1* (2), 554−564.

(29) Ju, E.; Dong, K.; Liu, Z.; Pu, F.; Ren, J.; Qu, X. Tumor Microenvironment Activated Photothermal Strategy for Precisely Controlled Ablation of Solid Tumors upon NIR Irradiation. *Adv. Funct. Mater.* **2015**, *25* (10), 1574−1580.

(30) Chen, Y.; Liu, X.; Yuan, H.; Yang, Z.; von Roemeling, C. A.; Qie, Y.; Zhao, H.; Wang, Y.; Jiang, W.; Kim, B. Y. S. Therapeutic Remodeling of the Tumor Microenvironment Enhances Nanoparticle Delivery. *Adv. Sci.* **2019**, *6* (5), 1802070.

(31) Cardone, R. A.; Casavola, V.; Reshkin, S. J. The Role of Disturbed PH Dynamics and the Na+/H+ Exchanger in Metastasis. *Nat. Rev. Cancer* **2005**, *5* (10), 786−795.

(32) Tang, Q.; Xiao, W.; Huang, C.; Si, W.; Shao, J.; Huang, W.; Chen, P.; Zhang, Q.; Dong, X. PH-Triggered and Enhanced Simultaneous Photodynamic and Photothermal Therapy Guided by Photoacoustic and Photothermal Imaging. *Chem. Mater.* **2017**, *29* (12), 5216−5224.

(33) Wang, Z.; Upputuri, P. K.; Zhen, X.; Zhang, R.; Jiang, Y.; Ai, X.; Zhang, Z.; Hu, M.; Meng, Z.; Lu, Y.; Zheng, Y.; Pu, K.; Pramanik, M.; Xing, B. PH-Sensitive and Biodegradable Charge-Transfer Nanocomplex for Second near-Infrared Photoacoustic Tumor Imaging. *Nano Res.* **2019**, *12* (1), 49−55.

(34) Miki, K.; Kojima, K.; Oride, K.; Harada, H.; Morinibu, A.; Ohe, K. PH-Responsive near-Infrared Fluorescent Cyanine Dyes for Molecular Imaging Based on PH Sensing. *Chem. Commun.* **2017**, *53* (55), 7792−7795.

(35) Spence, G. T.; Hartland, G. V.; Smith, B. D. Activated Photothermal Heating Using Croconaine Dyes. *Chem. Sci.* **2013**, *4* (11), 4240.

(36) Guha, S.; Shaw, G. K.; Mitcham, T. M.; Bouchard, R. R.; Smith, B. D. Croconaine Rotaxane for Acid Activated Photothermal Heating and Ratiometric Photoacoustic Imaging of Acidic PH. *Chem. Commun.* **2016**, *52* (1), 120−123.

(37) Harmatys, K. M.; Battles, P. M.; Peck, E. M.; Spence, G. T.; Roland, F. M.; Smith, B. D. Selective Photothermal Inactivation of Cells Labeled with Near-Infrared Croconaine Dye. *Chem. Commun.* **2017**, *53* (71), 9906−9909.

(38) McGarraugh, H. H.; Liu, W.; Matthews, B. P.; Smith, B. D. Croconaine Rotaxane Dye with 984 Nm Absorption: Wavelength-

Selective Photothermal Heating. *Eur. J. Org. Chem.* **2019**, *2019* (21), 3489−3494.

(39) Chen, Q.; Liu, X.; Zeng, J.; Cheng, Z.; Liu, Z. Albumin-NIR Dye Self-Assembled Nanoparticles for Photoacoustic PH Imaging and PH-Responsive Photothermal Therapy Effective for Large Tumors. *Biomaterials* **2016**, *98*, 23−30.

(40) Tang, L.; Zhang, F.; Yu, F.; Sun, W.; Song, M.; Chen, X.; Zhang, X.; Sun, X. Croconaine Nanoparticles with Enhanced Tumor Accumulation for Multimodality Cancer Theranostics. *Biomaterials* **2017**, *129*, 28−36.

(41) Valluru, K. S.; Willmann, J. K. Clinical Photoacoustic Imaging of Cancer. *Ultrasonography* **2016**, *35* (4), 267−280.

(42) Banerjee, S. S.; Aher, N.; Patil, R.; Khandare, J. Poly(Ethylene Glycol)-Prodrug Conjugates: Concept, Design, and Applications. *J. Drug Delivery* **2012**, *2012*, 1−17.

(43) Makadia, H. K.; Siegel, S. J. Poly Lactic-Co-Glycolic Acid (PLGA) as Biodegradable Controlled Drug Delivery Carrier. *Polymers (Basel, Switz.)* **2011**, *3* (3), 1377−1397.

(44) Nance, E.; Zhang, C.; Shih, T.-Y.; Xu, Q.; Schuster, B. S.; Hanes, J. Brain-Penetrating Nanoparticles Improve Paclitaxel Efficacy in Malignant Glioma Following Local Administration. *ACS Nano* **2014**, *8* (10), 10655−10664.

(45) Bi, Y.; Liu, L.; Lu, Y.; Sun, T.; Shen, C.; Chen, X.; Chen, Q.; An, S.; He, X.; Ruan, C.; Wu, Y.; Zhang, Y.; Guo, Q.; Zheng, Z.; Liu, Y.; Lou, M.; Zhao, S.; Jiang, C. T7 Peptide-Functionalized PEG-PLGA Micelles Loaded with Carmustine for Targeting Therapy of Glioma. *ACS Appl. Mater. Interfaces* **2016**, *8* (41), 27465−27473.

(46) Samkange, T.; D'Souza, S.; Obikeze, K.; Dube, A. Influence of PEGylation on PLGA Nanoparticle Properties, Hydrophobic Drug Release and Interactions with Human Serum Albumin. *J. Pharm. Pharmacol.* **2019**, *71* (10), 1497−1507.

(47) Ma, L.; Chen, Q.; Ma, P.; Han, M. K.; Xu, Z.; Kang, Y.; Xiao, B.; Merlin, D. IRGD-Functionalized PEGylated Nanoparticles for Enhanced Colon Tumor Accumulation and Targeted Drug Delivery. *Nanomedicine* **2017**, *12* (16), 1991−2006.

(48) Fang, X.; Wu, X.; Li, Z.; Jiang, L.; Lo, W.; Chen, G.; Gu, Y.; Wong, W. Biomimetic Anti-PD-1 Peptide-Loaded 2D FePSe 3 Nanosheets for Efficient Photothermal and Enhanced Immune Therapy with Multimodal MR/PA/Thermal Imaging. *Adv. Sci.* **2021**, *8* (2), 2003041.

(49) Zhan, C.; Huang, Y.; Lin, G.; Huang, S.; Zeng, F.; Wu, S. A Gold Nanocage/Cluster Hybrid Structure for Whole-Body Multispectral Optoacoustic Tomography Imaging, EGFR Inhibitor Delivery, and Photothermal Therapy. *Small* **2019**, *15* (33), 1900309.

(50) Spessard, G. O.; Streitwieser, A.; Heathcock, C. H. Introduction to Organic Chemistry. *J. Chem. Educ.* **1977**, *54* (6), A294.

(51) Ahmed, R.; Tariq, M.; Ahmad, I. S.; Fouly, H.; Fakhar-I-Abbas; Hasan, A.; Kushad, M. Poly(Lactic- Co -Glycolic Acid) Nanoparticles Loaded with Callistemon Citrinus Phenolics Exhibited Anticancer Properties against Three Breast Cancer Cell Lines. *J. Food Qual.* **2019**, *2019*, 1−12.